Check for updates

Preparation of mesoporous nanosphere SiO₂@TiO₂ composite materials and the photocatalytic degradation performance of different dyes

Wenqian Wu, [ID] [a] Weiye Yang, [ID] *[a] Jiuming Zhong,*[a] Hongyan Peng,[ab] Lijian Meng [ID] [c] and Shihua Zhao [ID] *[abd]

In this research, anatase-phase SiO₂@TiO₂ spherical photocatalysts were fabricated by the sol–gel method. Comprehensive characteization was performed through SEM, XRD, BET, XPS, PL, and UV-vis spectroscopy to elucidate the materials' morphology, crystal structure, composition, and optical properties. The photocatalytic performance was assessed through degradation rate of Rhodamine B (RhB). The catalyst annealed at 550 °C for 5 h exhibited exceptional activity and degraded 99.75% of RhB under UV light in 40 minutes, revealing a performance surpassing most literature reports. Notably, it retained over 83% efficiency after four cycles, attesting to its robust stability. Moreover, the annealing time exerted little effect on the photocatalytic activity of the photocatalyst. The free radical trapping experiment suggested that under visible light, hydroxyl radicals (˙OH) dominated RhB degradation, while holes (h⁺) and superoxide radicals (˙O₂⁻) contributed auxiliary roles. Furthermore, the impact of calcination parameters (temperature, duration), and catalyst addition amount, on the degradation of RhB, and the degradation ability of different pollutants was also systematically evaluated. These findings provide valuable insights for optimizing photocatalyst preparation and application.

1. Introduction

With the rapid development of industrialization and urbanization, environmental pollution in China has become increasingly severe, especially organic pollutants in water bodies, which pose a serious threat to ecosystems and human health.[1,2] Traditional pollutant treatment methods, such as adsorption,[3] flocculation,[4] and biodegradation,[5,6] have issues such as low efficiency, secondary pollution, or difficulty in thorough mineralization.[7] Simultaneously, the continuous consumption of fossil fuels has made the problem of energy shortage more prominent, and the development of new energy is urgent. Solar energy is a renewable energy source that is abundant, clean, pollution-free, and not limited by geography.[8–11] In the photocatalytic process, photocatalysts (such as TiO₂,[12] g-C₃N₄,[13–15] and ZnO[16–19]) absorb the energy of solar radiation and generate electron hole pairs, which then decompose organic pollutants into carbon dioxide, water, and small molecule inorganic materials through redox reactions.[20,21] Solar driven photocatalytic technology, with its outstanding advantages of renewability, low cost, and no secondary pollution, has become the core path for dealing with environmental pollution and energy shortages, in line with the concept of green and sustainable development.[22–24]

Among numerous photocatalytic materials, TiO₂ has attracted widespread attention because of its unique properties such as non-toxicity, low cost, high reactivity, and long-term stability against chemical and photo corrosion, as well as its application prospects in photocatalysis,[25,26] solar cells,[27] cosmetics,[28,29] and lithium-ion batteries.[30] However, it still faces a series of critical challenges in practical applications.[31] For example, (1) the absorption spectrum is narrow, leading to insufficient utilization of solar energy. Notably, TiO₂ can only be excited by light with a wavelength less than or equal to 387 nm (ultraviolet radiation), which accounts for only 5% of the total solar energy.[32] There is still a large amount of light energy that has not been utilized, and ultraviolet radiation poses a radiation hazard. (2) The probability of electron–hole recombination is high, whereas the quantum efficiency is low.[33] The quantum efficiency of conventional TiO₂ is only about 4%, with a maximum of no more than 10%. This can be explained as follows. The recombination of electrons and holes in the bulk phase and surface limits the application of photocatalytic technology and makes it difficult to compete economically with conventional environmental protection technologies. (3) TiO₂

*a*College of Physics and Electronic Engineering, Hainan Normal University, Haikou, 571158, China. E-mail: zsh@hainnu.edu.cn; haha_weiye@163.com; hnnuwdzjm@163.com

*b*The Innovation Platform for Academicians of Hainan Province, Haikou, Hainan Province, 571158, China

*c*CIETI/ISEP, Polytechnic of Porto, Rua Dr António Bernardino de Almeida, 4249-015 Porto, Portugal

*d*State Key Laboratory of Tropic Ocean Engineering Materials and Materials Evaluation, 570228, Haikou, China

catalysts in the form of nanoparticles have a small particle size and are prone to agglomeration during use, rendering recovery difficult.[34,35] While immobilization technology can solve the separation problem, it significantly reduces the specific surface area and the number of active sites, bringing about poor photocatalytic performance and secondary pollution of photocatalysts. (4) TiO_2 catalysts have poor adsorption performance due to their hydrophilic surface and lack of specific adsorption sites.[36,37] The chemical functional groups on the surface of TiO_2 catalysts are primarily hydroxyl groups and a small amount of oxygen vacancies, lacking a large number of microporous and mesoporous structures, as well as specific functional groups that can form strong interactions with organic compounds. Additionally, the strong hydrophilicity of the TiO_2 catalysts' surface contributes to a large number of active sites, such as hydroxyl and oxygen vacancies on the surface that tend to interact with water molecules rather than adsorb organic pollutants. Therefore, its adsorption capacity for organic compounds is limited. Many researchers have demonstrated the limitations of TiO_2 in photocatalysis, and by introducing SiO_2, composite catalysts can effectively improve these limitations, thereby enhancing photocatalytic efficiency. Camposeco, R. et al.[38] demonstrated that pure TiO_2 nanotubes have fewer acidic sites on their surface, limited hydroxyl adsorption capacity, and restricted adsorption and degradation efficiency for Rhodamine B. By loading 3 wt% SiO_2, the surface area was successfully increased and the formation of Brönsted acid sites on the surface of titanium dioxide nanotubes was promoted, thereby improving the photocatalytic and adsorption properties of titanium dioxide nanotubes. In the Nd-SiO_2 – TiO_2 nanocomposite prepared by Li et al.,[39] SiO_2 played a key role. The addition of SiO_2 not only inhibits crystal growth and the transformation of TiO_2 from anatase to rutile, but also enhances the adsorption of organic compounds, slows down the recombination rate of electron hole pairs, extending the photocatalyst light response to the visible region.

At present, the improvement of research around these issues can greatly enhance the possibility and practical value of photocatalytic technology in practical applications while expanding its corresponding application fields. Thus, optimizing and improving TiO_2 catalysts is a hot topic in the research field.

Silicon dioxide (SiO_2) is an inorganic non-metallic material with good chemical stability, high temperature resistance, non-toxicity, non-corrosiveness, and other characteristics. It has a wide range of sources and is inexpensive. Benefiting from its high surface area, it is widely applied in catalysis,[40–42] separation,[43] drug delivery,[44–47] coatings,[48,49] and microelectronics.[50] The composite photocatalyst prepared by loading nano TiO_2 on SiO_2 as a carrier fully utilizes the pollution removal and self-cleaning properties of titanium dioxide, as well as the adsorption and mechanical properties of silicon dioxide.[51] This composite material increases its specific surface area, improves photocatalytic efficiency, and enhances the stability and practicality of the material.[52] This provides direction for the development of cheaper and more efficient photocatalytic materials, demonstrating enormous application potential and broad development prospects.[53]

Various methods have been employed to prepare TiO_2 and SiO_2 composite samples with different morphologies and structures for the degradation of various dyes.[54–58] Hu et al.[59] adopted the catalytic hydrolysis method to prepare the SiO_2@-TiO_2 composite catalyst for the photocatalytic degradation of methylene blue (MB), and explored the photocatalytic performance of the material. With the biological resource rice husk (RH) as a biological template, Wang et al.[60] prepared mesoporous materials SiO_2@TiO_2 photocatalyst and discussed the RH derivatives SiO_2@TiO_2 photocatalytic degradation of Rhodamine B by photocatalysts. He et al.[61] prepared thermally stable SiO_2-doped mesoporous anatase titanium dioxide by the a templating method and evaluated the photocatalytic activity of the samples by degrading Rhodamine 6G (Rh 6G) solution under ultraviolet irradiation. Fu et al.[62] synthesized core–shell through the hydrothermal method and investigated the effect of different molar ratios of Ti/Si on the photocatalytic activity of methylene blue (MB) and phenol by the prepared SiO_2@TiO_2 nanoparticles (CSTNs). These studies suggest that the addition of SiO_2 not only delays the transition of TiO_2 crystal phase from anatase to rutile but also increases its specific surface area, improves adsorption performance, and suppresses the recombination of photogenerated carriers. Consequently, SiO_2@TiO_2 composite materials improve the efficiency and stability of photocatalytic degradation. In the past, the research work on SiO_2@TiO_2 composites mostly focused on exploring the influence of a single variable on photocatalytic degradation or enhancing the degradation efficiency of specific dyes. Nevertheless, it lacked comprehensiveness in exploring the influence of multiple factors on photocatalytic degradation.

In this study, the SiO_2@TiO_2 spheres with anatase phase were prepared by the sol–gel method as a photocatalyst, and various crystal properties of the photocatalyst were systematically investigated. The photocatalytic activity of the SiO_2@TiO_2 spheres was evaluated with Rhodamine B (RhB) as a target pollutant. A detailed discussion was conducted on the effects of calcination temperature, calcination time, and catalyst addition amount, on the degradation of RhB, and the degradation ability of different pollutants was also systematically evaluated. The intensive study of the role and degradation mechanism of active substances in the photocatalytic process lays a comprehensive theoretical foundation for optimizing the preparation conditions and applications of photocatalysts. Specifically, this study determined the optimal degradation conditions, improved photocatalytic efficiency, and curtailed energy consumption, providing theoretical support for practical applications.

2. Experimental section

2.1 Materials

Tetraethyl orthosilicate (TEOS): Sourced from Aladdin Co., Ltd, with a purity of ≥99%.

Titanium isopropoxide (TIP): Supplied by Macklin Co., Ltd, with a purity of 95%.

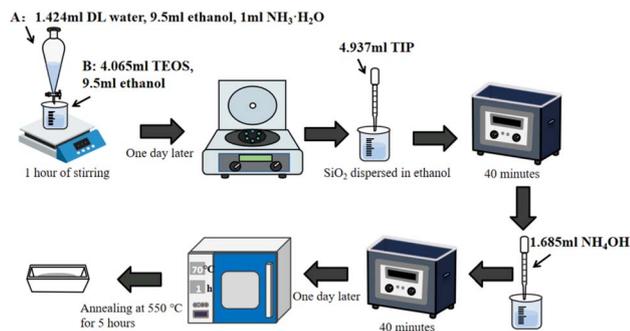Titanium dioxide (TiO_2): Obtained from Macklin Co., Ltd, with a purity of 99%.

Fig. 1 Schematic diagram of the experimental preparation process.

Ethanol (C_2H_6O): Supplied by Xilong Scientific Co., Ltd, with a purity of ≥99%.

Ammonium solution ($NH_3·H_2O$): obtained from Xilong Scientific Co., Ltd with a purity of 25–28%.

2.2 Synthesis of $SiO_2@TiO_2$ nanoparticle

2.2.1. Synthesis of SiO_2 spheres. Monodisperse SiO_2 spheres were synthesized as the carrier material through the Stöber method.[63] Specifically, 1 ml of ammonia water (catalyst), 1.424 ml of deionized water, and 9.5 ml of anhydrous ethanol were combined in a beaker to form solution A. Separately, solution B was prepared by mixing 4.065 ml of tetraethyl orthosilicate (TEOS) with 9.5 ml of anhydrous ethanol. Subsequently, solution A was added dropwise into solution B under continuous low-speed stirring. The reaction mixture was stirred for 1 hour and subsequently allowed to stand undisturbed for 24 hours. Next, the resulting suspension was centrifuged and washed three times with anhydrous ethanol. Finally, the SiO_2 powder obtained was vacuum dried at 70 °C.

2.2.2. Synthesis of $SiO_2@TiO_2$ composite materials. The $SiO_2@TiO_2$ composite was synthesized as follows. First, monodisperse SiO_2 powder (prepared previously) was dispersed in 19 ml of anhydrous ethanol. Subsequently, 4.937 ml of titanium isopropoxide (TIP) was added. The mixture was sonicated for 40 minutes and then reacted with 1.685 ml of ammonia solution for an additional 40 minutes. Afterward, the mixture was left undisturbed for 24 hours. The resulting product was dried at 70 °C and calcined in a muffle furnace at 550 °C for 5 hours. The $SiO_2@TiO_2$ sample with different preparation conditions was obtained by adjusting the annealing temperature(450 °C, 550 °C, 650 °C, 750 °C) and time (3 h, 5 h, 7 h). The schematic diagram of $SiO_2@TiO_2$ preparation is illustrated in Fig. 1.

3. Results and discussion

3.1 XRD of $SiO_2@TiO_2$

$SiO_2@TiO_2$ composite material was characterized by XRD to explore its crystal structure, phase composition, and crystal orientation. Fig. 2 presents XRD diagrams of SiO_2, TiO_2, and $SiO_2@TiO_2$ catalysts obtained by annealing at different temperatures for 5 h and $SiO_2@TiO_2$ catalysts obtained by annealing at 550 °C for different times. Fig. 2(a) exhibits the XRD diagram of SiO_2, TiO_2, and $SiO_2@TiO_2$ catalysts obtained by annealing at different temperatures for 5 h. Specifically, SiO_2 only has
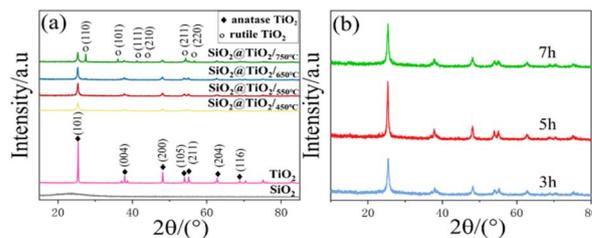

Fig. 2 XRD diagrams of (a) SiO_2, TiO_2, and $SiO_2@TiO_2$ catalysts obtained by annealing at different temperatures for 5 h; (b) $SiO_2@TiO_2$ catalysts obtained by annealing at 550 °C for different times.

a significant peak at 15° ∼30°, reflecting that SiO_2 is an amorphous structure.[64] Compared with the standard card of anatase TiO_2, the diffraction peaks of TiO_2 and composite sample $SiO_2@TiO_2$ at $2\theta = 25.2°$, 37.6°, 47.9°, 53.7°, 54.9°, 62.5°, and 68.59° corresponded to the (101), (004), (200), (105), (211), (204), and (116) crystal planes of anatase, respectively.[64] Compared to pure TiO_2, the addition of SiO_2 reduces the diffraction peak intensity of the composite sample and decreases the crystallinity of TiO_2. When the annealing temperature reached 750 °C, in addition to the anatase TiO_2 diffraction peak, rutile TiO_2 diffraction peaks appeared at $2\theta = 27.4°$, 36.0°, 41.2°, 44.0°, 54.3°, and 56.6°, corresponding to the (110), (101), (111), (210), (211), and (220) crystal planes of rutile type, respectively. In other words, some TiO_2 underwent a phase transition. Generally, TiO_2 experienced the phase transition from anatase to rutile when the calcination temperature reached 400–650 °C.[65–69] In contrast, the $SiO_2@TiO_2$ sample in the figure did not present the rutile phase until 750 °C. This suggests that the addition of SiO_2 microspheres can delay the occurrence of this transition.[60] The mechanism of adding SiO_2 to inhibit the formation of the rutile phase includes the following: 1. After doping with SiO_2, new chemical bonds (Ti–O–Si) emerge, indicating that some Si^{4+} replaces Ti^{4+} in the TiO_2 lattice, forming a substitutional solid solution. This ionic substitution disrupts the originally ordered lattice structure of TiO_2, leading to lattice distortion and strain energy. The distortion effect significantly hinders the diffusion of Ti^{4+} and O^{2-} ions, which is crucial for the transformation of the anatase lattice into the rutile lattice. Impeded diffusion directly suppresses the nucleation and growth of the rutile phase.[70] Li et al.[71] prepared titanium dioxide-silica composite nanoparticles by the sol–gel-hydrothermal method and the sol–gel method. The results demonstrate that the addition of silica affected the crystal phase transition of titanium dioxide and that the addition of a small amount of silica prevented the formation of a rutile phase. Fig. 2(b) exhibits the XRD patterns of $SiO_2@TiO_2$ annealed at 550 °C at different times. As observed from the figure, the diffraction peak intensity of $SiO_2@TiO_2$ catalyst first increased and then decreased with the increasing annealing time. The diffraction peak shape was the highest and sharpest when the annealing time was 5 h, specifying that the sample had preferable crystallinity.

3.2 SEM

$SiO_2@TiO_2$ composites were characterized by SEM and EDS to observe the micro-surface morphology of $SiO_2@TiO_2$
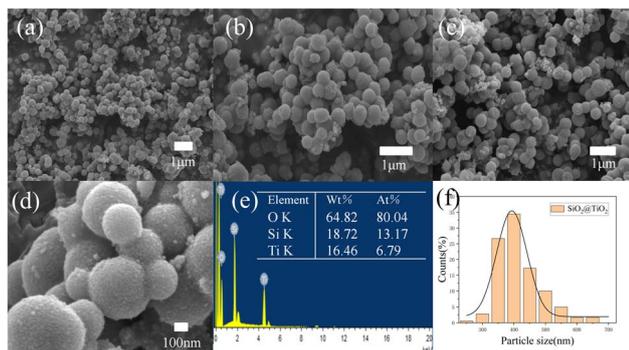
Fig. 3 (a–d) SEM images of $SiO_2@TiO_2$; (e) EDS spectrum; (f) particle size distribution curve.

Fig. 4 (a) N_2 adsorption–desorption isotherms; (b–d) pore size distribution curves of $SiO_2@TiO_2$, SiO_2, TiO_2.

composites and the shape, dispersion, surface defects, and detected elements of the microstructure. Fig. 3 shows SEM, EDS, and Particle size distribution curve images of $SiO_2@TiO_2$ composite materials. Fig. 3(a–d) depicts the SEM images of $SiO_2@TiO_2$. As shown in Fig. 3(a–d), the prepared product is a SiO_2 rough sphere with a diameter of several hundred nanometers and a large number of TiO_2 particles loaded on the surface. Surface roughness usually produces more pores [as shown in Fig. 3(d)]. The higher the roughness, the larger the specific surface area of the catalyst, which expands the contact area between the dye and the catalyst surface. The more exposed active adsorption sites (such as hydroxyl and oxygen vacancies on the TiO_2 surface), the more interface reaction sites are provided for the reaction between photogenerated carriers and dye molecules, reducing the probability of recombination of photogenerated electron hole pairs and significantly improving the degradation rate of Rhodamine B by the catalyst. Fig. 3(e) presents the EDS spectrum of $SiO_2@TiO_2$. The figure demonstrates only Si, Ti, and O elements and no other elements. Thus, the purity of the prepared material was verified, and TiO_2 particles successfully grew on the surface of SiO_2. Fig. 3(f) illustrates the particle size distribution curve of $SiO_2@TiO_2$, with the average particle size of 393 ± 5 nm.

3.3 BET

Mesoporous materials refer to porous materials with pore sizes ranging from 2 nanometers to 50 nanometers.[72] They have a highly ordered pore structure, a large specific surface area, adjustable pore size, and a rich pore structure.[73–76] Mesoporous materials not only significantly improve the light capture efficiency by extending the photon path to excite more photo generated carriers, but also shorten the diffusion distance of photo generated carriers from the bulk phase to the surface active sites, effectively suppressing the recombination of electron hole pairs and expanding the contact area with Rhodamine B dye molecules. Together, they enhance the photocatalytic degradation efficiency of the catalyst for dyes. BET (Brunauer–Emmett–Teller) characterization was employed to evaluate the specific surface area and pore structure of $SiO_2@TiO_2$ composites, so as to better understand and optimize the performance of materials.
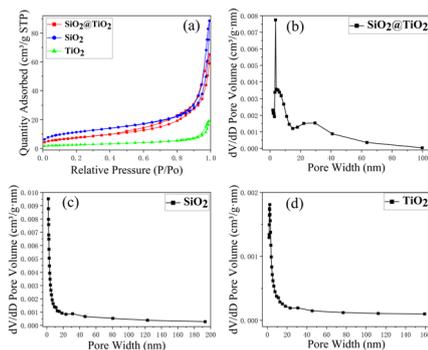
Fig. 4(a) exhibits the N_2 adsorption–desorption isotherms. The adsorption isotherm curves of SiO_2, TiO_2, and $SiO_2@TiO_2$ are type IV curves, revealing mesoporous structures in these three materials.[77] Fig. 4(b–d) suggests that the pore size of $SiO_2@TiO_2$, SiO_2, and TiO_2 were mainly centered at the range of 2–60 nm, 1–10 nm, and 2–10 nm, respectively. Most of the SiO_2 is in a microporous structure, while $SiO_2@TiO_2$ and TiO_2 samples are mostly in a mesoporous structure. The pore size distribution of the three materials was calculated by the BJH model, and the order of pore size was: $SiO_2 > SiO_2@TiO_2 > TiO_2$. Table 1 accounts for the specific surface area and BJH adsorption average pore size data of SiO_2, TiO_2, and $SiO_2@TiO_2$. As observed from the table, the introduction of SiO_2 enlarged the specific surface area from 9.3990 m^2 g^{-1} of pure TiO_2 to 27.5646 m^2 g^{-1} of $SiO_2@TiO_2$. A larger specific surface area can provide more adsorption centers and photocatalytic reaction centers.[78] This contributes to the photoelectric conversion process, the generation of more reactive oxygen species, and the adsorption contact between the material and the pollutant, thereby improving the photocatalytic performance.[79] Moreover, the addition of an appropriate amount of SiO_2 increased the acid sites on the surface of TiO_2 and thus reinforced the photocatalytic activity.[80] Notably, the increase in surface acidic sites brought about more adsorption sites, allowing for the adsorption of more hydroxide ions.[78] Hydroxide ions acted as hole traps to prevent electron–hole recombination, leading to higher quantum yield and thereby the enhanced photocatalytic activity of TiO_2.[78]

3.4 XPS

With the purpose of better analyzing the elemental composition of $SiO_2@TiO_2$ composite materials and the chemical state of specific elements, XPS characterization was performed to obtain more comprehensive and in-depth material surface

Table 1 BET specific surface area and pore size parameters of the catalyst

Sample	SBET/m^2 g^{-1}	BJH pore size/nm	Pore volume (cm^3 g^{-1})
SiO_2	41.0308	14.5642	0.136876
TiO_2	9.3990	12.6485	0.029710
$SiO_2@TiO_2$	27.5646	13.7469	0.100730

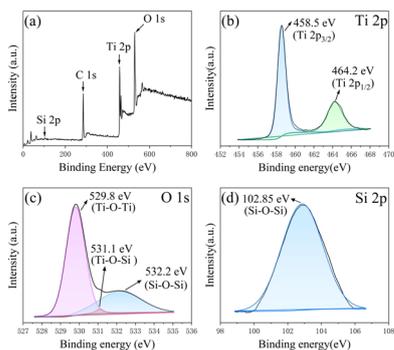**Fig. 5** (a) The full spectrum of $SiO_2@TiO_2$; (b) high-resolution narrow spectrum of Ti element; (c) O element, and (d) Si element.

information. Fig. 5(a) presents the full spectrum of $SiO_2@TiO_2$. The Si 2p, C 1s, Ti 2p, and O 1s orbitals in the figure corresponded to peaks at binding energies of 103.11, 284.81, 458.56, and 529.81 eV, respectively, verifying the presence of Si, C, Ti, and O elements.[87] Moreover, C was an impurity element introduced during the sample testing process. Fig. 5(b–d) exhibits the high-resolution narrow spectrum of Ti, O, and Si elements, respectively. As observed from Fig. 5(b), the narrow spectrum of Ti 2p can be divided into two peaks located at 458.5 and 464.2 eV, which were associated with Ti $2p_{3/2}$ and Ti $2p_{1/2}$, respectively.[88,89] The peak between Ti $2p_{3/2}$ and Ti $2p_{1/2}$ lines was *ca.* 5.7 eV, suggesting the existence of the Ti^{4+} oxidation state.[90–92] Fig. 5(c) reveals that the narrow spectrum of O 1s can be divided into three peaks located at 532.2, 531.1, and 529.8 eV, which correspond to Si–O–Si bonds, Ti–O–Si bonds, and Ti–O–Ti bonds, respectively.[61] Numerous researchers have demonstrated (as shown in Table 2) that the binding energy of the O 1s peak of pure SiO_2 is typically located at 532.6, corresponding to Si–O–Si bonds. The binding energy of the Si 2p peak is usually located at 103.4 eV, corresponding to the Si–O–Si bond. The binding energy of the O 1s peak of pure TiO_2 is usually located at 529.3, corresponding to the Ti–O–Ti bond. The binding energy of the Ti 2p peak is around 458.2 eV and 464 eV, corresponding to Ti $2p_{3/2}$ and Ti $2p_{1/2}$. In $SiO_2@TiO_2$ composite materials, which possess the binding energy of SiO_2 and TiO_2, there is also a new phenomenon where Ti^{4+} partially replaces Si^{4+} sites in SiO_2 lattice, or Si^{4+} is embedded at the edge of TiO_2 lattice, forming stable Ti–O–Si covalent bonds through oxygen atom bridging. The presence of the Ti–O–Si bond can effectively inhibit the phase transition between anatase and rutile, and the anatase phase is more favorable for photocatalytic reaction than the rutile phase.[93–95] Simultaneously, the existence of the Ti–O–Si bond reflects that the composite material has a TiO_2/SiO_2 semiconductor heterostructure,[96] which can effectively promote the separation of photogenerated electron transfer, inhibit the

recombination of electrons and holes, and increase the photocatalytic ability.[81] In Fig. 5(d), the peak at 102.85 eV was related to Si–O–Si, indicating that the material contains silica.[89,86]

To sum up, there is a strong interaction between silica nanospheres and titanium dioxide particles at the interface of nanoheterostructures.[91]

3.5 UV-vis spectral of $SiO_2@TiO_2$

The UV-vis diffuse reflectance spectra and optical band gap determine the light absorption characteristics and the generation efficiency of photo-generated charge carriers of photocatalysts, respectively. UV-vis diffuse reflectance spectra reflect the light absorption characteristics. Catalysts absorb photons, generate photo-generated charge carriers, and trigger photocatalytic reactions. The light absorption ability can directly influence the efficiency of photocatalytic reactions. The optical band gap defines the photon energy range that photocatalysts can absorb, influencing their response to various light wavelengths. The narrower the bandgap, the longer the wavelength of light that the photocatalytic material can absorb and the more photons can be utilized. The absorbed visible light photons are captured and converted into energy. After the catalyst absorbs light energy, it excites electrons to transition from the valence band to the conduction band, generating more photo generated carriers (electron hole pairs).[97] The effective separation and transport mechanism of photogenerated charge carriers enables them to migrate to the reaction sites on the catalyst surface to participate in chemical reactions, thereby enhancing photocatalytic activity. Therefore, the efficiency of light energy utilization has been improved. UV-vis diffuse reflectance and optical band gap are crucial factors influencing photocatalytic performance. Therefore, the UV-vis diffuse reflectance and optical band gap of $SiO_2@TiO_2$ composite material were characterized in this study.

Fig. 6 shows the UV-vis diffuse reflectance spectra and optical band gap diagrams of TiO_2 and $SiO_2@TiO_2$. Fig. 6(a) presents the UV-vis diffuse reflectance spectra of TiO_2 and $SiO_2@TiO_2$ catalysts annealed at different temperatures. As observed from the figure, all samples had strong ultraviolet absorption at around 200 nm to 400 nm, attributed to titanium dioxide nanoparticles.[98] Therefore, the prepared $SiO_2@TiO_2$ composite sample is suitable for absorbing all UVA, UVB, and UVC radiation.[99] The peak around 230 nm corresponded to the ligand-to-metal charge transfer (LMCT) from O^{2-} to Ti^{4+} in the presence of tetrahedrally coordinated Ti^{4+} ions.[64,100–103] Fig. 6(b) illustrates the optical band gap diagram of the photocatalyst. The band gap energy was obtained by plotting the relationship between $(\alpha h v)^{1/2}$ and photon energy (hv).[64] Concerning crystalline titanium dioxide, the theoretical band gap between the conduction band and the valence

Table 2 Binding energy of the measured photoemission peaks (eV)

Sample	Ti 2p		Si 2P	O 1s	Reference
SiO_2	—	—	Si–O–Si	Si–O–Si	81–83
TiO_2	Ti $2p_{1/2}$	Ti $2p_{3/2}$	—	Ti–O–Ti	Ref. 84 and 85
$SiO_2@TiO_2$	Ti $2p_{1/2}$	Ti $2p_{3/2}$	Si–O–Si	Si–O–Si, Ti–O–Ti, Ti–O–Si	Ref. 81 and 86

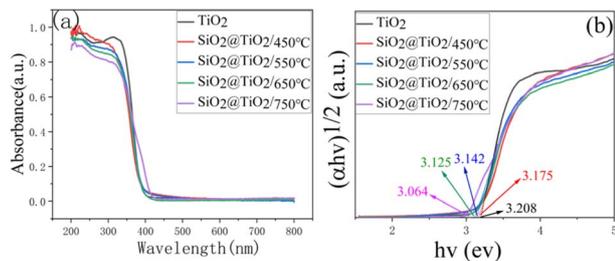**Fig. 6** (a) UV–vis diffuse reflectance spectra and (b) optical band gap of TiO$_2$ and SiO$_2$@TiO$_2$ catalysts annealed at different temperatures.
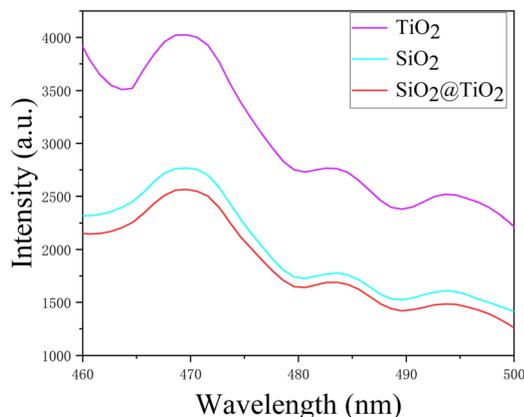

Fig. 7 PL spectra of the catalyst (excitation wavelength of 222 nm).

band of anatase was 3.2 eV. Compared with pure TiO$_2$, the band gap energy of SiO$_2$@TiO$_2$ catalyst decreased, suggesting that the energy required for electron transition dropped, making it easier to absorb photons in a wider frequency range and generate more electron–hole pairs.

3.6 PL of SiO$_2$@TiO$_2$

Fluorescence spectroscopy is commonly employed to investigate the separation efficiency of holes and electrons in semiconductor materials, and the fluorescence intensity mainly depends on the combination of electrons and holes.[104,105] Fig. 7 displays the photoluminescence spectra of SiO$_2$, TiO$_2$, and SiO$_2$@TiO$_2$ catalysts under 222 nm excitation. All the samples revealed a luminescence peak near 470 nm. Moreover, the SiO$_2$@TiO$_2$ composite catalyst exhibited a lower fluorescence intensity, implying that the photoinduced excited electrons and holes can be effectively inhibited, thereby improving the photocatalytic activity.

4. Photocatalytic activity

4.1 Photocatalytic degradation experiment

Four typical organic dyes, rhodamine B (RhB), methylene blue (MB), malachite green (MG), and rhodamine 6G (Rh 6G), were used to simulate wastewater pollutants, so as to evaluate the photocatalytic degradation effect of SiO$_2$@TiO$_2$ composites on rhodamine B (RhB) and different dyes under different preparation conditions.[106,107] There are three reasons for setting these dyes as target pollutants for photocatalytic degradation

research. First, these dyes have clear toxicity and environmental persistence, and are typical recalcitrant organic pollutants.[108,109] Second, it has significant absorption peaks and fluorescence characteristics in spectral analysis, allowing it to monitor concentration changes in real-time easily through UV-visible spectroscopy. This can facilitate the study of photocatalytic reaction kinetics and mechanisms of these dyes. Finally, it is representative in actual industrial wastewater and widely applied in industries such as textiles, printing and dyeing, and papermaking. Its treatment is urgently needed, and research outcomes readily translate into practical applications.[110,111] Therefore, choosing Rhodamine B (RhB), Methylene Blue (MB), Malachite Green (MG), and Rhodamine 6G (Rh 6G) as model wastewater pollutants has scientific research value and practical environmental significance.

Experimental details are presented as follows. First, a 250 W ultraviolet lamp served as the light source. Prior to illumination, 50 mg of catalyst was dispersed in 50 mL of aqueous dye solution (10 mg L^{-1}) and magnetically stirred in the dark for 30 min to establish adsorption–desorption equilibrium. Afterward, the UV lamp was activated. The samples were collected at 10-minute intervals and centrifuged to remove catalyst particles. The supernatant was analyzed by UV-vis spectroscopy. Subsequently, degradation efficiency was determined from the reduction in characteristic absorption peak intensity (the characteristic absorption peak of Rhodamine B usually appeared around 554 nm).

Furthermore, RhB was selected as the model pollutant to identify the dominant reactive oxygen species (ROS) involved in the photocatalytic degradation mechanism. Free radical trapping experiments were conducted under identical photocatalytic conditions by 1,4-benzoquinone (BQ) for superoxide radicals ($^{\bullet}O_2^-$), potassium iodide (KI) for holes (h$^+$), and isopropanol (IPA) for hydroxyl radicals ($^{\bullet}OH$). In each test, 1 mM of scavenger was introduced into the dye solution before reaction initiation. The identical experimental procedure described above was followed.

4.2 Photocatalytic activity

Fig. 8 shows the photocatalytic degradation efficiency and reaction kinetics diagrams of SiO$_2$, TiO$_2$, and SiO$_2$@TiO$_2$. Fig. 8(a) exhibits a photocatalytic degradation efficiency diagram of SiO$_2$, TiO$_2$, and SiO$_2$@TiO$_2$ samples annealed at 550 °C for 5 h. As shown in the figure, after 30 minutes of dark reaction adsorption–desorption equilibrium, the adsorption rates of the SiO$_2$@TiO$_2$ composite catalyst were consistently higher than those of pure SiO$_2$ and TiO$_2$, reaching over 40%. Compared to pure SiO$_2$ or pure TiO$_2$, the SiO$_2$@TiO$_2$ composite material typically exhibits higher adsorption rates. This is attributed to the introduction of TiO$_2$, which adds strong adsorption active sites to the composite, while SiO$_2$ acts as a carrier to optimize the dispersion and pore structure of TiO$_2$. Consequently, the SiO$_2$@TiO$_2$ composite material possesses a larger specific surface area and a mesoporous structure, providing more adsorption active sites. The synergy between these two components enhances both adsorption capacity and
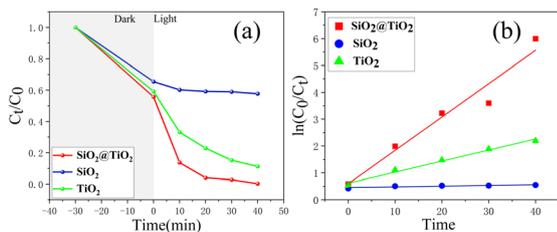
Fig. 8 (a) Photocatalytic degradation efficiency diagram of SiO_2, TiO_2, and $SiO_2@TiO_2$ samples annealed at 550 °C for 5 h, and (b) reaction kinetics diagram.

strength, thereby improving the overall adsorption effect.[112–114] Specifically, the photocatalytic activity of the $SiO_2@TiO_2$ catalyst was higher than that of pure SiO_2 and TiO_2. The degradation rate of the RhB solution by $SiO_2@TiO_2$ catalyst under ultraviolet light irradiation for 40 min reached 99.75%. The degradation rates of RhB solution by SiO_2 and TiO_2 under ultraviolet light irradiation for 40 min were 42.85% and 88.81%, respectively.

Fig. 8(b) illustrates a reaction kinetics diagram. The photocatalytic degradation reaction kinetics model adopts the first-order reaction kinetics equation, expressed as follows:[115,116]

$$-\ln(C_t / C_0) = kt$$

where k denotes the first-order apparent degradation rate constant (min^{-1}); C_t indicates the concentration of reactants at time t ($mg\ L^{-1}$); C_0 represents the initial concentration of the reactant ($mg\ L^{-1}$); t signifies the reaction time (min). In Fig. 8(b), the $SiO_2@TiO_2$ composite sample revealed the fastest degradation rate.

The complexity of photocatalytic degradation experiments mainly stems from the diversity of reaction environments and conditions, which collectively influence the performance and degradation efficiency of photocatalysts. Therefore, the effects of calcination parameters (temperature, duration), catalyst addition amount, and pollutant identity on degradation efficiency were investigated in our study. Specifically, this study determined the optimal degradation conditions, improved photocatalytic efficiency, and curtailed energy consumption, providing theoretical support for practical applications. Fig. 9(a) illustrates the photocatalytic degradation efficiency diagram of RhB by $SiO_2@TiO_2$ annealed at different temperatures for 5 h. The photocatalytic degradation efficiency diagram of $SiO_2@TiO_2$ catalyst first increased and then decreased with the growing annealing temperature. When the annealing temperature was 550 °C, the degradation rate of the RhB solution reached 99.75% under UV irradiation for 40 min. The reason is that the suitable temperature for calcination (450–550 °C) can promote the decomposition and crystallization of the precursor with increasing temperature, increase the crystallinity of anatase phase, enhance the diffraction peak, and improve the photocatalytic degradation efficiency. The mesoporous structure of titanium dioxide calcined at high temperatures (650–750 °C) may be damaged, and the crystal phase may transition from the anatase phase to the rutile phase, leading to a decrease in photocatalytic activity.[117–120] This is consistent with the above
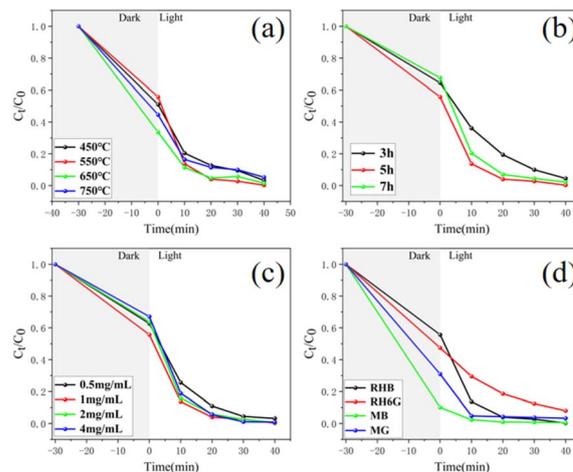

Fig. 9 (a) The photocatalytic degradation efficiency diagram of annealed at different temperatures for 5 h, (b) the photocatalytic degradation efficiency diagram of annealed at 550 °C for different times, (c) the photocatalytic degradation efficiency diagram of adding different amounts of $SiO_2@TiO_2$ catalyst prepared by annealing at 550 °C for 5 hours, and (d) the photocatalytic degradation efficiency diagram on different dyes by adding 1 mg mL^{-1} $SiO_2@TiO_2$ catalyst prepared by annealing at 550 °C for 5 hours.

XRD characterization results. Fig. 9(b) exhibits the photocatalytic degradation efficiency diagram of RhB by $SiO_2@TiO_2$ catalyst annealed at 550 °C for different times. As observed from the figure, the annealing time exerted little effect on the photocatalytic activity of the photocatalyst,[92,120] and the degradation rate of RhB with three different annealed times exceeded 95% within 40 min. Fig. 9(c) illustrates the photocatalytic degradation efficiency diagram of adding different amounts of $SiO_2@$-TiO_2 catalyst (prepared by annealing at 550 °C for 5 hours) addition. The photocatalytic degradation efficiency first increased and then decreased with the growing catalyst addition. When the amount of catalyst added was 1 mg mL^{-1}, the degradation rate of the RhB solution reached the highest of 99.75% under ultraviolet light irradiation for 40 min. This was attributed to the fact that the amount of catalyst added was less, and fewer reactive oxygen species were produced.[120] The ability to absorb catalyst photons reached saturation as the amount of catalyst increased to a critical value. The number of holes and electrons no longer increased, resulting in a relatively stable degradation rate.[120] Some experiments are performed with other pollutants, such as rhodamine 6G (Rh6G), methylene blue (MB), and malachite green (MG), to determine the feasibility of the catalyst for degrading other dyes with different chemical structures. Based on the optimal degradation conditions mentioned above, we will conduct photocatalytic degradation experiments on different dyes by adding 1 mg mL^{-1} $SiO_2@TiO_2$ photocatalyst (prepared by annealing at 550 °C for 5 hours), as shown in Fig. 9(d). Fig. 9(d) exhibits the order of degradation efficiency of the four different dyes as follows: RHB > MB > MG > RH6G.[92] Methylene blue (MB) and malachite green (MG) are cationic dyes that can easily adsorb onto negatively charged catalyst surfaces through electrostatic interactions, but excessive adsorption can block the active sites.[121–126] Rhodamine 6G
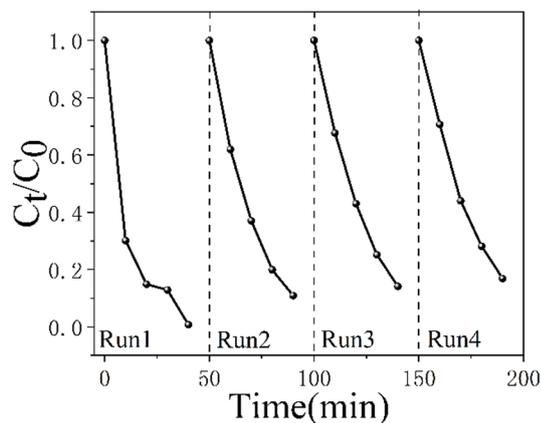
Fig. 10 The four-cycle photocatalytic degradation rate diagram of RhB by the SiO$_2$@TiO$_2$ composite catalyst.

(RH6G) is a weak cationic dye with poor adsorption efficiency,[127,128] and Rhodamine B (RhB) is an amphoteric dye due to its molecular structure containing both positively charged diethylamino groups and the negative charge from carboxyl ionization. Rhodamine B (RhB) exhibits high efficiency in photocatalytic degradation, mainly due to the following reasons: (1) Rhodamine B (RhB), as an amphoteric dye, can bind to catalysts through diethylamino groups while avoiding the problem of excessive adsorption blockage of cationic dyes (such as MB/MG).[129] (2) Rhodamine B (RhB) has a large molecular structure, complex conjugated systems (chromophore), and high photosensitivity, which enables it to more effectively absorb photons and generate excited state electrons.[130] These excited-state electrons can be transferred to the conduction band of the photocatalyst, thereby promoting the generation of reactive oxygen species (ROS) and the degradation of dye molecules. (3) Rhodamine B (RhB) molecules adsorb onto the surface of SiO$_2$@TiO$_2$ materials through positively charged diethylamino groups, making them more susceptible to surface holes and reactive oxygen species (ROS) attacks, resulting in continuous deethylation reactions and the formation of the characteristic blue shift effect of dye molecules.[131–133] At the same time, they undergo direct degradation of the chromophore system. Under the synergistic effect of adsorption and reactive oxygen species(ROS), RhB molecules undergo degradation reactions simultaneously on the material surface and in the solution system, accelerating the degradation rate of RhB molecules. Therefore, the photocatalytic reaction rate of Rhodamine B (RhB) is faster than that of methylene blue (MB),

malachite green (MG), and rhodamine 6G (RH6G) (as shown in Fig. 9). Under the irradiation of an ultraviolet lamp, the degradation rate of the four dyes both reached more than 92%. Therefore, the catalyst has a good application prospect in the treatment of various organic pollutants.

Fig. 10 demonstrates the four-cycle photocatalytic degradation rate diagram of rhodamine B (RhB) by the SiO$_2$@TiO$_2$ composite catalyst. The degradation rates of each cycle were 99.26%, 89.05%, 85.83%, and 83.09%, respectively. Although the degradation rate gradually decreased with each cycle, it remained above 83%, specifying excellent structural stability.

Table 3 presents a comparison of the efficiency of other studies on the degradation of rhodamine B (RhB). Table 3 reveals that the SiO$_2$@TiO$_2$ photocatalyst prepared in this work exerted a strong photocatalytic degradation effect of 99.75% after 40 min, which was superior to the degradation efficiency reported in other studies.

5. Possible mechanisms

The photocatalytic performance of reactive oxygen species (ROS) during the degradation process was conducted to discover the role of reactive oxygen species (ROS) in the degradation process by various scavengers, so as to better understand the reaction mechanism of SiO$_2$@TiO$_2$ nanocomposite photocatalytic materials. Therefore, the SiO$_2$@TiO$_2$ photocatalyst was employed to rhodamine B (RhB) degradation under ultraviolet light irradiation with potassium iodide (KI) as a hole (h$^+$) cavenger, isopropanol (IPA) as a hydroxyl radical ($^\cdot$OH) scavenger, and 1,4-benzoquinone (BQ) as a superoxide radical $^\cdot$O$_2^-$ scavenger.

Fig. 11 depicts the free radical trapping experimental diagram of the RhB degradation. As suggested in Fig. 11, compared with the sample without the addition of a scavenger, the sample with potassium iodide (KI) to remove holes (h$^+$) exhibited a certain degree of inhibitory effect on photodegradation, and its effect is insignificant. The addition of 1,4-benzoquinone (BQ) to the sample for scavenging superoxide radicals ($^\cdot$O$_2^-$) weakened the degradation efficiency of rhodamine B (RhB) from 99.75% to 76.22% and hence inhibited the photocatalytic degradation effect. However, the degradation efficiency of rhodamine B (RhB) decreased from 99.75% to 56.22% after the addition of isopropanol (IPA) to scavenge hydroxyl radicals ($^\cdot$OH), reflecting a significant inhibitory effect on photocatalytic degradation. Therefore, hydroxyl radicals ($^\cdot$OH) are the main reactive oxygen species in the photocatalytic

Table 3 Photocatalytic degradation of RhB by catalysts in other studies

Catalyst	Concentration of catalyst and dye	Light source	K min^{-1}	Photocatalytic degradation(%)	Reference
TiO$_2$/SiO$_2$	50 mg 100 mL^{-1} (10 mg L^{-1})	Visible-light	0.1067	98.6% after 40 min	120
SiO$_2$@TiO$_2$	0.3 mg mL^{-1} (20 mg L^{-1})	300 W Hg lamp	0.04654	82.2% after 35 min	134
TiO$_2$/SiO$_2$	0.005 g 250 mL^{-1} (10 mg L^{-1})	15 W visible-light lamps of 900 lumens	0.018	100% after 210 min	135
TiO$_2$@SiO$_2$-Ag	1 mg mL^{-1} (10 mg L^{-1})	Sunlight	0.02186	92% after 60 min	136
SiO$_2$@TiO$_2$	1 mg mL^{-1} (10 mg L^{-1})	UV light	0.124	99.75% after 40 min	This work
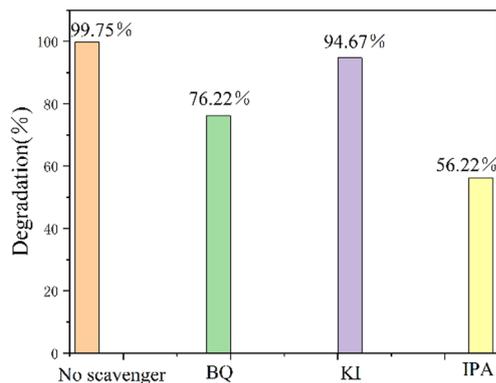
Fig. 11 Free radical trapping experimental diagram of the RhB degradation.

Fig. 12 SiO$_2$@TiO$_2$ schematic diagram of photocatalytic degradation mechanism.

degradation of rhodamine B (RhB), followed by holes (h$^+$) and superoxide radicals ($\cdot$O$_2$$^-$).

The results of the free radical trapping experiment reveal the specific roles of different active species in photocatalytic reactions ($\cdot$O$_2$$^-$, h$^+$, $\cdot$OH), assisting in refining the reaction pathway in the mechanism diagram. Hence, the photocatalytic mechanism diagram of the generation, separation, transfer, and interaction process of photo-generated carriers (electrons and holes) with reactants is illustrated in detail.
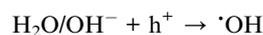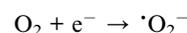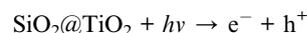
RhB has both positively charged diethylamino groups and the negative charge from carboxyl ionization in its molecular structure, making it an amphiprotic dye. The surface of SiO$_2$ is rich in silanol, which exhibits a negative potential due to its easy deprotonation in aqueous solutions, thus enabling effective adsorption of molecules with positively charged groups in the solution. In contrast, TiO$_2$ has a surface potential approaching neutrality and lacks such adsorption capability. The composite catalytic material of SiO$_2$@TiO$_2$ features SiO$_2$ loaded with TiO$_2$ crystals *via* Ti–O–Si bonds. Due to the differing crystal structures of the two solid phases, phase interfaces inevitably contain defects and distortions, resulting in a richer abundance of surface hydroxyl groups and a higher negative potential.

Fig. 12 depicts the schematic diagram of the photocatalytic degradation mechanism.[135] As observed from the figure, the electrons in the valence band of the SiO$_2$@TiO$_2$ catalyst were excited to the conduction band under UV light irradiation, leaving holes in the valence band, thereby forming a photogenerated electron–hole pair. The electron (e$^-$) in the conduction band (CB) can easily react with dissolved O$_2$ in water to generate superoxide radicals ($\cdot$O$_2$$^-$). Meanwhile, the photo-generated hole (h$^+$) in the valence band (VB) can directly react with OH$^-$ or surface-bound water to generate hydroxyl radicals ($\cdot$OH). The generated active substances $\cdot$O$_2$$^-$, $\cdot$OH) continue to attack RhB.[137] In the photodegradation of rhodamine B, two different mechanisms are involved the direct degradation of the chromophoric system and the successive deethylation of the four ethyl groups.[138–142] Both mechanisms are independent and can proceed side-by-side. The deethylation route shows that RhB molecules adsorb onto the surface of composite materials through positively charged diethylamino groups, making diethylamino groups more susceptible to ROS attack and

undergoing continuous deethylation reactions to form *N*-deethylated intermediates (DRhB, NRhB), which exhibit the characteristic blue shift effect of dye molecules. These intermediates are then further degraded into organic acids or alcohols under the influence of ROS, and finally degraded into H$_2$O, CO$_2$, and so on. Due to the free radical capture experiment showing that hydroxyl radicals ($\cdot$OH) are the main reactive oxygen species in the photocatalytic degradation of Rhodamine B (RhB) (as shown in Fig. 11), it is speculated that chromophores are preferentially attacked by ROS, leading to dye cleavage and the formation of hydroxylation intermediates. Under the continuous oxidation of ROS, it continues to be converted into low molecular weight intermediate products until it is degraded into inorganic compounds such as CO$_2$, H$_2$O, *etc*.[143,144] The chemical reactions involved in the degradation process are as follows:[145]

$$SiO_2@TiO_2 + h\nu \rightarrow e^- + h^+$$

$$O_2 + e^- \rightarrow \cdot O_2^-$$

$$H_2O/OH^- + h^+ \rightarrow \cdot OH$$

$$\cdot O_2^-/\cdot OH + RhB \rightarrow Intermediates \rightarrow CO_2 + H_2O$$

6. Conclusion

In this study, anatase-phase SiO$_2$@TiO$_2$ spherical photocatalysts were successfully synthesized by the sol–gel method. SiO$_2$ incorporation significantly improved TiO$_2$ performance by forming Ti–O–Si bonds, delaying anatase-to-rutile phase transition, increasing specific surface area (providing more adsorption/reaction sites), decreasing bandgap energy (lowering electron transition barriers), and reducing fluorescence intensity (indicating suppressed electron–hole recombination). These synergistic effects collectively enhanced charge separation and photocatalytic activity. The photocatalytic experiments suggest that SiO$_2$@TiO$_2$ annealed at 550 °C for 5 h achieved 99.75% degradation of RhB under UV irradiation within 40 min, surpassing most reported values. The material

retained over 83% efficiency after four recycling tests, confirming robust structural stability. Scavenger experiments unveil that hydroxyl radicals ($^{\bullet}$OH) served as the dominant active species in RhB degradation under visible light, with holes (h^+) and superoxide radicals ($^{\bullet}O_2^-$) playing secondary roles. These findings demonstrate that $SiO_2@TiO_2$ composites exhibit outstanding photocatalytic activity and stability, offering a promising pathway for developing cost-effective, high-performance photocatalytic materials with significant application potential.

Author contributions

Wenqian Wu: conceptualization (lead); software (lead); data curation (lead); writing – original draft (lead); methodology (lead). Weiye Yang: supervision (equal); writing – review & editing (equal); methodology (equal). Jiuming Zhong: supervision (equal); writing – review & editing (equal). Hongyan Peng: supervision (equal); writing – review & editing (equal). Lijian Meng: supervision (equal); writing – review & editing (equal). Shihua Zhao: conceptualization (supporting); supervision (equal); writing – review & editing (equal); funding acquisition (lead); investigation (lead); methodology (equal); project administration (equal); resources (lead).

Conflicts of interest

The authors declare that they have no known competing financial interests or personal relationships that could have appeared to influence the work reported in this paper.

Data availability

The data that support the findings of this study are available on request from the corresponding author, upon reasonable request.

Acknowledgements

References

1 L. Lin, H. R. Yang and X. C. Xu, *Front. Environ. Sci. Eng.*, 2022, **10**, 880246.

2 V. Saxena, *Water, Air, Soil Pollut.*, 2025, **236**, 73.

3 Y. T. Yu and H. W. Huang, *Chem. Eng. J.*, 2023, **453**, 139755.

4 N. Loukili, L. Jossic, D. Blésès, M. Oliveira, Y. Fayolle, P. Ginisty, N. Elkissi, A. Magnin and Y. Rharbi, *Colloids Surf., A*, 2024, **702**, 134975.

5 S. J. Li, M. J. Cai, Y. P. Liu, C. C. Wang, R. Y. Yan and X. B. Chen, *Adv. Powder Mater.*, 2023, **2**, 100073.

6 S. S. Mohanty and A. Kumar, *Sci. Rep.*, 2021, **11**, 13390.

7 Mp Shah, *Adv. Recycling Waste Manage.*, 2016, **2**, 115.

8 N. S. Seroka, R. Taziwa and L. Khotseng, *Materials*, 2022, **15**(15), 5338.

9 A. Qazi, F. Hussain, N. A. Rahim, G. Hardaker, D. M. Alghazzawi, K. B. Shaban and K. Haruna, *IEEE Access*, 2019, **7**, 63837–63851.

10 S. E. Kondolot and I. Erdal, *RSC Adv.*, 2023, **13**, 12244–12269.

11 E. Fabian, E. Munonyedi, A. U. John, N. O. B. Rejoice, O. Julius and M. Julius, *Bull. Natl. Res. Cent.*, 2024, **48**, 29.

12 W. S. Jiang, X. P. Zong, X. Y. Wang and Z. C. Sun, *Chem. Res. Chin. Univ.*, 2020, **36**, 1097–1101.

13 J. N. Rao, Z. W. Cheng, H. Lv, Z. Peng, C. C. Han, F. Nemangwele and X. G. Ma, *Diamond Relat. Mater.*, 2025, **157**, 112478.

14 M. Z. Salmasi, A. Omidkar, H. Q. Ying and H. Song, *J. Environ. Chem. Eng.*, 2025, **13**, 117180.

15 W. X. Wang, S. J. Zhou, Y. Zhu and W. H. Li, *Chem. Eng. Sci.*, 2025, **315**, 121881.

16 C. A. Soto-Robles, O. Nava, L. Cornejo, E. Lugo-Medina, A. R. Vilchis-Nestor, A. Castro-Beltrán and P. A. Luque, *J. Mol. Struct.*, 2021, **1225**, 129101.

17 S. Venkatesan, S. Suresh, P. Ramu, J. Arumugam, S. Thambidurai and N. Pugazhenthiran, *Results Chem.*, 2022, **4**, 100637.

18 P. Lad, V. Pathak, A. B. Thakkar, P. Thakor, M. P. Deshpande and S. Pandya, *Braz. J. Phys.*, 2023, **53**(3), 63.

19 P. Liang, W. Y. Yang, H. Y. Peng and S. H. Zhao, *Molecules*, 2024, **29**, 5584.

20 X. H. He, Y. D. Yang, Y. H. Li, J. L. Chen, S. J. Yang, R. Liu and Z. F. Xu, *Appl. Surf. Sci.*, 2022, **599**, 153898.

21 S. Phanichphant, A. Nakaruk and D. Channei, *Appl. Surf. Sci.*, 2016, **387**, 214–220.

22 X. Li, J. Xie, C. J. Jiang, J. G. Yu and P. Y. Zhang, *Front. Environ. Sci. Eng.*, 2018, **12**(5), 1–32.

23 K. Sapkota, I. Lee, M. Hanif, M. Islam, J. Akter and J. Hahn, *Catalysts*, 2020, **10**, 297.

24 S. Sharma and S. Basu, *Sep. Purif. Technol.*, 2020, **231**, 115916.

25 A. Fujishima and X. T. Zhang, *C. R. Chim.*, 2005, **9**, 750–760.

26 L. Manmohan, S. Praveen and R. Chhotu, *Results Mater.*, 2022, **15**, 100308.

27 P. Suriya, M. Prabhu and K. Jagannathan, *Mater. Today: Proc.*, 2022, **65**, 100–105.

28 V. M. Virginia, A. Virginia, M. Aida, P. B. M. Fernanda, C. M. Florencia, P. M. Fernanda, Z. Ariana, B. M. Cecilia and S. C. M. Jazmin, *J. Photochem. Photobiol.*, 2023, **15**, 100173.

29 B. Marta, A. Elżbieta, K. Agata and G. Beata, *Molecules*, 2023, **28**, 645.

30 L. P. An, W. Z Li, J. Q. Wang, S. H. Liu, K. Jiao, L. H. Fan, J. Q. Liang, Z. Liu and Q. Du, *Appl. Energy*, 2024, **355**, 122272.

31 H. R. Dong, G. M. Zeng, L. Tang, C. Z. Fan, C. Zhang, X. X. He and Y. He, *Water Res.*, 2015, **79**, 128–146.

32 S. Yin, Q. W. Zhang, F. Saito and T. Sato, *Chem. Lett.*, 2003, **32**, 358–359.

33 Z. F. Bian, J. Zhu, S. H. Wang, Y. Cao, X. F. Qian and H. X. Li, *J. Phys. Chem. C*, 2008, **112**, 6258–6262.

34 B. Gao, P. S. Yap, T. M. Lim and T.-T. Lim, *Chem. Eng. J.*, 2011, **171**, 1098–1107.

35 S. Mallakpour and E. Nikkhoo, *Adv. Powder Technol.*, 2014, **25**, 348–353.

36 O. Allam, M. Maghsoodi, S. S. Jang and S. D. Snow, *ACS Appl. Mater. Interfaces*, 2024, **16**, 36215–36223.

37 C. Wang, R. K. Zhang, Y. C. Miao, Q. H. Xue, B. R. Yu, Y. Z. Gao, Z. G. Han and M. F. Shao, *Dalton Trans.*, 2021, **50**, 17911–17919.

38 R. Camposeco, S. Castillo, M. H. Reyes, I. M. Centeno and R. Zanella, *Top. Catal.*, 2020, **64**, 1–13.

39 J. l. Li, T. Liu, G. Z. Sui and D. S. Zhen, *J. Nanosci. Nanotechnol.*, 2015, **15**(2), 1408–1415.

40 B. Lin, C. Xue, X. Q. Yan, G. D. Yang, G. Yang and B. L. Yang, *Appl. Surf. Sci.*, 2015, **357**, 346–355.

41 S. J. Jian, L. Ran, Y. Q. Zhu, W. S. Yang, Y. F. Liu, H. Q. Yang, G. G. Duan and S. H. Jiang, *Compos. Commun.*, 2024, **49**, 101977.

42 E. Pakdel, W. A. Daoud, S. Seyedin, J. Wang, J. M. Razal, L. Sun and X. Wang, *Colloids Surf., A*, 2018, **552**, 130–141.

43 Z. Yang, M. Kei, H. George, M. Nirmalya, K. Tsutomu, K. Hiroki, K. Kazuyoshi and N. Kazuki, *J. Sep. Sci.*, 2015, **38**, 2841–2847.

44 M. A. Al Tahan, M. Marwah, H. E. Zein, S. A. Tahan and L. S. Aranguren, *Int. J. Pharm.*, 2025, **678**, 125656.

45 M. K. Sharma, N. Aggarwal, R. Kumar, J. J. Panda, C. Yu and A. K. Ganguli, *Microporous Mesoporous Mater.*, 2025, **391**, 113624.

46 M. I. Grini, C. Benbayer, S. S. Besbes and A. Elaissari, *Microporous Mesoporous Mater.*, 2025, **391**, 113603.

47 S. Bhattacharya, D. Chatterjee and A. Datta, *J. Drug Delivery Sci. Technol.*, 2025, **110**, 107068.

48 S. T. Cai, X. Chen, S. L. Wang, X. Q. Liao, Z. Chen and Y. Lin, *Chin. Chem. Lett.*, 2025, **36**(6), 110798.

49 B. Aïssa, M. I. Hossain, A. Zekri, A. A. Abdallah and V. B. Benito, *Sol. Energy*, 2025, **293**, 113485.

50 Ł. Laskowski, M. Laskowska, N. Vila, M. Schabikowski and A. Walcarius, *Molecules*, 2019, **24**, 2395.

51 Y. Hendrix, A. Lazaro, Q. Yu and J. Brouwers, *World J. Nano Sci. Eng.*, 2015, **05**, 161–177.

52 C. H. Kang, L. Q. Jing, T. Guo, H. C. Cui, J. Zhou and H. G. Fu, *J. Phys. Chem. C*, 2009, **113**(3), 1006–1013.

53 M. Pierpaoli, X. Zheng, V. Bondarenko, G. Fava and M. L. Ruello, *Environments*, 2019, **6**, 87.

54 J. Y. Yang, X. Y. Xu, Y. J. Liu, Y. Gao, H. B. Chen and H. M. Li, *Colloids Surf., A*, 2019, **582**, 123858.

55 Y. Jiang, Z. Jin, C. Chen, W. B. Duan, B. Liu, X. D. Chen, F. H. Yang and J. P. Guo, *RSC Adv.*, 2017, **7**, 12856–12870.

56 M. Urbashi, K. Mudrika and D. A. Suresh, *Appl. Surf. Sci.*, 2022, **576**, 151745.

57 W. H. Saputera, J. Rizkiana, W. Wulandari and D. Sasongko, *RSC Adv.*, 2020, **10**, 27713–27719.

58 L. Ryeri, K. Yogeenth, Y. S. Young, U. S. Ho, K. I. Keun and J. G. Young, *RSC Adv.*, 2017, **7**, 7469–7475.

59 S. Z. Hu, F. Y. Li and Z. P. Fan, *Bull. Korean Chem. Soc.*, 2012, **33**, 1895–1899.

60 W. Wang, H. Chen, J. J. Fang and M. Lai, *Appl. Surf. Sci.*, 2019, **467–468**, 1187–1194.

61 C. X. He, B. Z. Tian and J. L. Zhang, *J. Colloid Interface Sci.*, 2010, **344**, 382–389.

62 N. Fu, X. C. Ren and J. X. Wan, *J. Nanomater.*, 2020, **2020**, 1–11.

63 W. Stöber, A. Fink and E. Bohn, *J. Colloid Interface Sci.*, 1968, **26**, 62–69.

64 U. Mahanta, M. Khandelwal and A. S. Deshpande, *Appl. Surf. Sci.*, 2022, **576**, 151745.

65 Z. D. Xing and H. L. Xiang, *J. Mater. Res.*, 1998, **13**, 2556–2559.

66 J. Ovenstone and K. Yanagisawa, *Chem. Mater.*, 1999, **11**, 2770–2774.

67 K. S. P. Karunadasa and C. H. Manoratne, *J. Solid State Chem.*, 2022, **314**, 123377.

68 M. Lal, P. Sharma and C. Ram, *Optik*, 2021, **241**, 166934.

69 N. Wetchakun, B. Incessungvorn, K. Wetchakun and S. Phanichphant, *Mater. Lett.*, 2012, **82**, 195–198.

70 S. C. Wu, X. Luo, Y. F. Long, L. Zhang, B. J. Xu and R. Huang, *J. Mater. Eng.*, 2020, **48**(11), 99–107.

71 Z. J. Li, B. Hou, Y. Xu, D. Wu, Y. H. Sun, W. Hu and F. Deng, *J. Solid State Chem.*, 2005, **178**(5), 1395–1405.

72 Z. Zhou and M. Hartmann, *Chem. Soc. Rev.*, 2013, **42**, 3894.

73 C. Perego and R. Millini, *Chem. Soc. Rev.*, 2013, **42**, 3956–3976.

74 N. Linares, A. M. Silvestre-Albero, E. Serrano, J. Silvestre-Albero and J. García-Martínez, *Chem. Soc. Rev.*, 2014, **43**, 7681–7717.

75 L. L. Duan, C. Y. Wang, W. Zhang, B. Ma, Y. H. Deng, W. Li and D. Y. Zhao, *Chem. Rev.*, 2021, **121**, 14349–14429.

76 C. Li, Q. Li, Y. V. Kaneti, D. Hou, Y. Yamauchi and Y. Y. Mai, *Chem. Soc. Rev.*, 2020, **49**, 4681–4736.

77 Y. Li, Q. Q. Shen, R. F. Guan, J. B. Xue, X. G. Liu, H. S. Jia, B. S. Xu and Y. C. Wu, *J. Mater. Chem. C*, 2020, **8**, 1025–1040.

78 X. Z. Fu, L. A. Clark, Q. Yang and M. A. Anderson, *Environ. Sci. Technol.*, 1996, **30**, 647–653.

79 M. H. Zhang, L. Y. Shi, S. Yuan, Y. Zhao and J. H. Fang, *J. Colloid Interface Sci.*, 2009, **330**, 113–118.

80 W. Qiu, C. J. Ren, M. C. Gong, Y. Z. Hou and C. Yq, *Acta Phys. Chim. Sin.*, 2011, **27**, 1487–1492.

81 Y. Li, Y. Luo, B. Zhang, X. N. Tang and Y. F. Chen, *J. Inorg. Mater.*, 2019, **34**, 1325.

82 G. M. Bancroft, H. W. Nesbitt, R. Ho, D. M. Shaw, J. S. Tse and M. C. Biesinger, *Phys. Rev. B:Condens. Matter Mater. Phys.*, 2009, **80**, 075405.

83 M. E. Simonsen, C. Sønderby, Z. Li and E. G. Søgaard, *J. Mater. Sci.*, 2009, **44**, 2079–2088.

84 W. H. Cheng, C. D. Li, X. Ma, L. M. Yu and G. Y. Liu, *Mater. Des.*, 2017, **126**, 155–161.

85 Y. L. Lin, T. J. Wang and Y. Jin, *Powder Technol.*, 2002, **123**, 194–198.

86 D. M. Xu, H. M. Yu, Y. Qin, Y. Di, H. B. Jia, F. S. Li and J. Liu, *ACS Appl. Nano Mater.*, 2024, **7**, 2630–2638.

87 X. Y. Cao, X. N. Tang, H. Ma and Y. Y. Chen, *Rare Metal Mat. Eng.*, 2022, **51**, 3001–3012.

88 M. Wang, B. Gong, X. Yao, Y. Wang and R. N. Lamb, *Thin Solid Films*, 2006, **515**, 2055–2058.

89 C. Liu, D. Yang, Y. Jiao, Y. Tian, Y. G. Wang and Z. Y. Jiang, *ACS Appl. Mater. Interfaces*, 2013, **5**, 3824–3832.

90 W. Zhao, L. L. Feng, R. Yang, J. Zheng and X. G. Li, *Appl. Catal., B*, 2011, **103**, 181–189.

91 N. Guo, Y. M. Liang, S. Lan, L. Liu, G. J. Ji, S. C. Gan, H. F. Zou and X. C. Xu, *Appl. Surf. Sci.*, 2014, **305**, 562–574.

92 Z. Y. Yang, Y. L. Xu and S. J. Yang, *Russ. J. Appl. Chem.*, 2017, **89**, 2050–2060.

93 A. Nilchi, S. Janitabar-Darzi, A. R. Mahjoub and S. Rasouli-Garmarodi, *Colloids Surf., A*, 2010, **361**, 25–30.

94 S. J. Cheepborisutikul and M. Ogawa, *Inorg. Chem.*, 2023, **62**, 12166–12174.

95 V. D. Chinh, A. Broggi, L. Di Palma, M. Scarsella, G. Speranza, G. Vilardi and P. N. Thang, *J. Electron. Mater.*, 2017, **47**, 2215–2224.

96 C. Han, Y. P. Lei and Y. D. Wang, *J. Inorg. Mater.*, 2015, **30**, 1121.

97 X. F. Ning, S. G. Meng, X. L. Fu, X. J. Ye and S. F. Chen, *Green Chem.*, 2016, **18**, 3628–3639.

98 Y. Zhang, J. R. Chen, L. Hua, S. J. Li, X. X. Zhang, W. C. Sheng and S. S. Cao, *J. Hazard. Mater.*, 2017, **340**, 309–318.

99 G. Asghar, X. Dong, S. Chae, S. Saqlain, S. Oh, K. H. Choi, J. Jeon, C. Woo, T. Y. Kim, J. Ahn, H.-S. Oh, J.-H. Park, H. K. Yu and J.-Y. Choi, *Cryst. Growth Des.*, 2022, **23**, 256–262.

100 M. Anpo and J. M. Thomas, *Chem. Commun.*, 2006, **2006**, 3273–3278.

101 D. Zhao, S. Budhi, A. Rodriguez and R. T. Koodali, *Int. J. Hydrogen Energy*, 2010, **35**, 5276–5283.

102 S. Budhi, C.-M. Wu, D. Zhao and R. Koodali, *Catalysts*, 2015, **5**, 1603–1621.

103 R. Peng, D. Zhao, N. M. Dimitrijevic, T. Rajh and R. T. Koodali, *J. Phys. Chem. C*, 2011, **116**, 1605–1613.

104 X. Y. Zhou, Z. Y. Zhou, W. Q. Wu, W. Y. Yang, H. Y. Peng and S. H. Zhao, *PLoS One*, 2025, **20**, e0322559.

105 Q. Z. Luo, L. L. Bao, D. S. Wang, X. Y. Li and J. An, *J. Phys. Chem. C*, 2012, **116**, 25806–25815.

106 Z. Y. Zhou, W. Y. Yang, J. M. Zhong, H. Y. Peng and S. H. Zhao, *Molecules*, 2025, **30**(24), 4800.

107 Y. Y. Cai, X. C. Liu, W. Y. Yang, H. Y. Peng, L. J. Meng and S. H. Zhao, *RSC Adv.*, 2025, **15**, 49875–49888.

108 A. Vijeata, G. R. Chaudhary, S. Chaudhary and A. Umar, *Chemosphere*, 2023, **341**, 139946.

109 M.-A. Gatou, N. Bovali, N. Lagopati and E. A. Pavlatou, *Molecules*, 2024, **29**, 4299.

110 S. Shanmugam, H. Sekar, R. Govindarajan, A. Venkatesan, A. Samraj, R. Aruliah and G. Muthusamy, *J. Appl. Microbiol.*, 2022, **134**, lxac064.

111 A. Tkaczyk, K. Mitrowska and A. Posyniak, *Sci. Total Environ.*, 2020, **717**, 137222.

112 W. Y. Dong, C. W. Lee, X. C. Lu, Y. J. Sun, W. M. Hua, G. S. Zhuang, S. C. Zhang, J. M. Chen, H. Q. Hou and D. Y. Zhao, *Appl. Catal., B*, 2010, **95**, 197–207.

113 W. Chang, L. L. Yan, L. Bin and R. J. Sun, *Ceram. Int.*, 2017, **43**, 5881–5886.

114 C. C. Dong, J. H. Ji, Z. Yang, Y. F. Xiao, M. Y. Xing and J. L. Zhang, *Chin. Chem. Lett.*, 2019, **30**, 853–862.

115 N. R. Khalid, U. Mazia, M. B. Tahir, N. A. Niaz and M. A. Javid, *J. Mol. Liq.*, 2020, **313**, 113522.

116 S. Raha and M. Ahmaruzzaman, *Chem. Eng. J.*, 2020, **387**, 123766.

117 B. Aleksandra, W. Agnieszka, K. Ewelina and M. A. Waldemar, *Catalysts*, 2023, **13**, 186.

118 H. Zhang, S. J. Sun, H. Ding, T. R. Deng and J. Wang, *Mater. Sci. Semicond. Process.*, 2020, **115**, 105099.

119 N. Fu, H. J. Chen, R. H. Chen, S. Y. Ding and X. C. Ren, *Coatings*, 2023, **13**, 852.

120 Z. Y. Yang, G. Y. Shen, Y. P. He, X. X. Liu and S. J. Yang, *J. Porous Mater.*, 2015, **23**, 589–599.

121 A. Mohammadreza, F. Moslem, K. N. Mohammadreza and H. Aliasghar, *Sci. Rep.*, 2022, **12**, 20415.

122 A. Haleem, M. Ullah, S. U. Rehman, A. Shah, M. Farooq, T. Saeed, I. Ullah and H. Li, *Water*, 2024, **16**, 1588.

123 D. Doveiko, K. K. Ossowska and Y. Chen, *ACS Omega*, 2024, **9**, 4123–4136.

124 A. Celine, E. K. Riham and P. Digambara, *Mater. Chem. Phys.*, 2022, **277**, 125504.

125 S. X. Ge, B. B. Wang, D. P. Li, W. J. Fa, Z. Y. Yang, Z. Yang, G. Y. Jia and Z. Zheng, *Appl. Surf. Sci.*, 2014, **295**, 123–129.

126 A. J. Maira, K. L. Yeung, C. Y. Lee, P. L. Yue and C. K. Chan, *J. Catal.*, 2000, **192**, 185–196.

127 F. Songjie, G. Hao, W. Yumei and L. Jianhua, *J. Indian Chem. Soc.*, 2022, **99**, 100579.

128 G. K. Ramesha, A. V. Kumara, H. B. Muralidhara and S. Sampath, *J. Colloid Interface Sci.*, 2011, **361**, 270–277.

129 W. Rao, P. Piliouras, X. Wang, A. Guido, K. Kugler, B. Sieren, L. Wang, G. Lv and Z. Li, *Appl. Clay Sci.*, 2020, **197**, 105790.

130 Y. D. Liu, F. Chen, L. Sun, Z. Z. Zhang, S. Z. Chang, J. L. Zhang and B. Z. Tian, *Res. Chem. Intermed.*, 2023, **49**, 2417–2432.

131 R. Y. Guo, Y. Bao, X. Zheng, J. Chen, H. Yang, W. B Zhang, C. Liu and J. C. Xu, *ACS Appl. Mater. Interfaces*, 2023, **15**, 47447–47462.

132 Z. J. Ma, W. B. Chen, Z. L. Hu, X. Z. Pan, G. P. Dong, S. F. Zhou, M. Y. Peng, Y. Li, C. X. Liao, Q. L. Xiao and J. R. Qiu, *RSC Adv.*, 2013, **3**, 20132.

133 Z. He, S. G. Yang, Y. M. Ju and C. Sun, *J. Environ. Sci.*, 2009, **21**, 268–272.

134 Y. Bao, R. Y. Guo, M. Gao, Q. L. Kang and J. Z. Ma, *J. Alloys Compd.*, 2021, **853**, 157202.

135 M.-A. Gatou, E. Fiorentis, N. Lagopati and E. A. Pavlatou, *Water*, 2023, **15**, 2773.

136 P. Govindhan and C. Pragathiswaran, *J. Mater. Sci. Mater. Electron.*, 2016, **27**, 8778–8785.

137 L. J. Pei, X. M. Gu, Y. T. Zhang, J. Wang, H. Tan, P. F. Wang and Z. F. Zheng, *J. Environ. Chem. Eng.*, 2021, **9**, 105815.

138 S. Murcia-López, J. A. Navío and M. C. Hidalgo, *Appl. Catal. Gen.*, 2013, **466**, 51–59.

139 O. Merka, V. Yarovyi, D. W. Bahnemann and M. Wark, *J. Phys. Chem. C*, 2011, **115**, 8014–8023.

140 H. B. Fu, C. S. Pan, W. Q. Yao and Y. F. Zhu, *J. Phys. Chem. B*, 2005, **109**, 22432–22439.

141 F. Chen, J. C. Zhao and H. Hidaka, *Int. J. Photoenergy*, 2003, **5**, 209–217.

142 M. C. F. D. Cordoba, J. Matos, R. Montaña, P. S. Poon, S. Lanfredi, F. R. Praxedes, J. C. Hernández-Garrido, J. J. Calvino, E. Rodríguez-Aguado, E. Rodríguez-Castellón and C. O. Ania, *Catal. Today*, 2019, **328**, 125–135.

143 T. Rasheed, M. Bilal, H. M. N. Iqbal, S. Z. H. Shah, H. Hu, X. Zhang and Y. Zhou, *Environ. Technol.*, 2017, **39**, 1533–1543.

144 D. C. Ma, J. W. Tang, G. W. He and S. Pan, *Materials*, 2024, **17**, 957.

145 J. H. Li, C. M. Yang, C. F. Zhang, S. Zhang, X. H. Ma, X. J. Wu, T. Y. Wang, X. L. Yue and M. R. Chang, *Acta Photonica Sin.*, 2022, **51**, 0216001.